Transp Porous Med (2013) 98:15–34
DOI 10.1007/s11242-013-0123-4

Experimental Measurements of Stress and Chemical Controls on the Evolution of Fracture Permeability

Thomas P. McGuire · Derek Elsworth · Zvi Karcz

Received: 2 April 2012 / Accepted: 16 January 2013 / Published online: 7 February 2013

Abstract We explore how fracture permeability in confined tight carbonates evolves due to flow of reactive fluids. Core plugs of the Capitan Massive Limestone are saw-cut to form a smooth axial fracture that is subsequently roughened to control the fracture surface topography. Either distilled water or distilled water–ammonium chloride solutions are circulated through these plugs, where fracture roughness, inlet fluid pH, and confining stresses are controlled. Throughout the experiment we measure the fluid flow rate and chemical composition of the effluent fluid. Mass balance, conducted on the effluent fluid mass and on dissolved mineral components, independently constrains the mineral mass removal. We use an idealized lumped parameter model of asperity supported fractures undergoing simultaneous stress corrosion cracking-induced diffusion and free-face dissolution to infer theoretical rates of aperture loss or gain. This model incorporates the roles of confining stress, fracture contact area, and composition and reactivity of the permeating fluid while identifying zones of diffusion-dominated mass transfer within the fracture. These theoretical rates of aperture strain are compared to those inferred from the experimentally determined permeability evolution and permeating fluid mineral mass balance. By measuring in regimes of both increasing and decreasing permeability we quantitatively constrain the transition between fracture-gaping and fracture-closing modes of behavior. We parameterize this transition in permeability evolution by the ratio of mechanically to chemically controlled dissolved mass fluxes. The transition from regimes of closing to regimes of gaping occurs at unity ($\chi \approx 1$) when stress and chemically driven mass fluxes are theoretically equal.

T. P. McGuire (✉)
Department of Energy and Mineral Engineering and G3 Center, Pennsylvania State University, 230A Hosler Building, University Park, PA, USA

D. Elsworth
Department of Energy and Mineral Engineering and G3 Center, Pennsylvania State University, 231 Hosler Building, University Park, PA, USA

Z. Karcz
Delek Energy, 12 Aba Even Street, Ackerstein Tower D, 9th Floor, P.O. Box 12837, 46725 Herzeliya , Isreal

Keywords Carbonate fracture · Fracture permeability evolution · Stress corrosion cracking · Fracture dissolution · Fracture strain

1 Introduction

The extremely low matrix permeability of some tight carbonate reservoirs ($< 10^{-17}$ m^2) (Volery et al. 2010) cause the flow through them to be controlled by fractures. The Damkohler number and Peclet number are often used to describe the relative magnitudes of free-face dissolution (Kalia and Balakotaiah 2009; Detwiler and Rajaram 2007; Yasuhara and Elsworth 2006; Panga et al. 2005; Dijk and Berkowitz 1998; Siemers and Dreybrodt 1998; Daccord et al. 1993; Hoeffner and Fogler 1988) and precipitation (Yasuhara and Elsworth 2006; Dijk and Berkowitz 1998) that occur during flow through fractures. Relative magnitudes of pressure solution, stress corrosion, and the above mechanisms result in fracture permeability that either increases (Kalia and Balakotaiah 2009; Detwiler and Rajaram 2007; Panga et al. 2005; Siemers and Dreybrodt 1998; Daccord et al. 1993; Hoeffner and Fogler 1988) or decreases (Zhang et al. 2011; Yasuhara and Elsworth 2006; Dijk and Berkowitz 1998) with time. Simulations of fluid–rock interactions explore free-face dissolution (Kalia and Balakotaiah 2009; Detwiler and Rajaram 2007; Yasuhara and Elsworth 2006; Panga et al. 2005; Siemers and Dreybrodt 1998; Daccord et al. 1993; Hoeffner and Fogler 1988), pressure solution (Yasuhara and Elsworth 2006; Yasuhara et al. 2004, 2003), stress corrosion (Zhang et al. 2011), or both free-face dissolution and pressure solution (Yasuhara and Elsworth 2006). Experiments exploring fluid–rock interactions are similarly focused on free-face dissolution effects (Detwiler and Rajaram 2007; Daccord et al. 1993; Detwiler 2008; Polak et al. 2004; Durham et al. 2001) or pressure solution effects (Polak et al. 2004; Croizé et al. 2010; Zhang et al. 2010; Donohue et al. 2009; Karcz et al. 2008; Polak et al. 2003) with very few exploring implications of stress corrosion cracking (Karcz et al. 2008; Yasuhara et al. 2011) or both pressure solution and free-face dissolution occurring simultaneously (Polak et al. 2004).

2 Mechanisms Implicated in Permeability Evolution

Breakthrough of dominant flow channels, also known as wormholing, has been extensively studied through experimentation (Detwiler and Rajaram 2007; Daccord et al. 1993; Polak et al. 2004) and modeling (Kalia and Balakotaiah 2009; Detwiler and Rajaram 2007; Panga et al. 2005; Daccord et al. 1993; Hoeffner and Fogler 1988). Both approaches show that at low flow rates wormhole formation is inhibited due to free-face dissolution limited to the entry face of the sample whereas at high flow rates their formation is inhibited by uniform corrosion of the entire fracture. Between these two extremes highly conductive channels reaching through the samples form due to free-face dissolution of the walls of an initial through-going pore-scale tube or channel (Panga et al. 2005). Larger numbers of these through-going pore-scale channels, commonly quantified by higher initial fracture roughness or an increased size or number of fracture heterogeneities, has been numerically predicted to increase the propensity for channeling (Kalia and Balakotaiah 2009).

Current theories indicate that the increase in permeability caused by fracture channeling may be mitigated by the preferential dissolution of highly stressed asperities that prop the fracture (Yasuhara et al. 2011; Yasuhara and Elsworth 2006; Yasuhara et al. 2004; Polak et al. 2003). This pressure solution becomes the dominant mechanism of water–rock interaction when effective stresses on the fracture-propping asperities exceeds the critical stress and

the pore fluid is saturated—disabling simultaneous dissolution of unstressed fracture walls (Croizé et al. 2010; Zhang et al. 2010). Some of the more recent studies that examine the pressure solution of calcite (Croizé et al. 2010; Zhang et al. 2010; Donohue et al. 2009) and halite (Karcz et al. 2008) have shown significant pressure solution-induced strain effects, some at relatively low stresses (Yasuhara et al. 2011; Zhang et al. 2011, 2010; Donohue et al. 2009). This interaction of dissolution and brittle failure at sub-critical stresses, termed hereafter as *stress corrosion cracking*, can be nearly six orders of magnitude faster than free-face dissolution at low temperatures, and may contribute to the effective loss in hydraulic aperture of the fracture (Zhang et al. 2011). We theorize that stress corrosion cracking induces fracture compaction during flow of under-saturated fluid due to diffusion-controlled mass transport from fracture contacts due to enhanced surface area from stress corrosion cracking.

To decipher the mixed effects of free-face dissolution and the proposed stress-corrosion-induced compaction in stressed reactive porous media we conducted controlled experiments on repeatable fractures in a tight vuggy carbonate. We measure initial fracture surface roughness along with fluid and dissolved mineral mass efflux during flow-through experiments. These observations are used to independently constrain key mineral redistribution mechanisms in our lumped parameter model. They also serve to constrain threshold limits of key parameters that signal the transitions from reaction dominated to stress-dominated regimes as parameterized in the mass flux ratio.

3 Experimental Set-up

We conduct flow-through experiments on cylindrical samples of artificially fractured limestone. The evolution of permeability is independently constrained by continuous measurements of fluid and dissolved mass efflux and by pre- and post-test measurements of fracture morphology by white light interferometry.

3.1 Flow-through Permeability Tests

Flow-through experiments are conducted on 5.0 cm long by 2.5 cm diameter artificially fractured core samples of Capitan Massive Limestone (CML), a massive vuggy limestone, maintained at a temperature of 293 K. Single artificial fractures are created in each sample by saw-cutting the sample axially, and subsequently roughening the surfaces with either a "rough" 60 grit ceramic (average grain size of 423 μm resulting in a root mean square fracture roughness of 8.27 μm) or a "fine" 150 grit ceramic (average grain size of 169 μm resulting in a root mean square fracture roughness of 3.80 μm) prior to each experiment. Separate experiments on freshly prepared samples are conducted for each and every experimental condition. The initial effective permeability of the fractured samples prepared with 60 grit and 150 grit average $\sim$ 174 and $\sim$ 4.0 mD, respectively, while the matrix permeability is $<<$ 1.0 mD. This low matrix permeability combined with identical-fractured sample preparation leads to insignificant variation in the initial permeability of identically prepared samples.

The fractured sample is placed between two stainless steel end-platens faced with flow distributors and sealed within a latex membrane. This composite sample assembly is then placed within a confining cell and plumbed for end-to-end fluid flow driven by pressurized nitrogen from an upstream to a downstream reservoir (Fig. 1).

Table 1 Lists the experimental conditions of our suite of experiments.

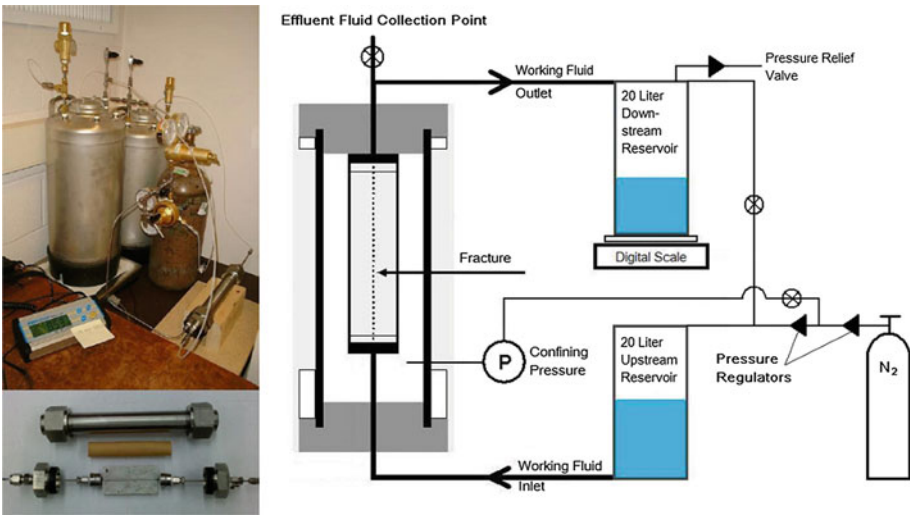

Fig. 1 View and schematic of the experimental set-up including an internal view of the flow-through core holder

Table 1 List of experiments

Experiment number	Stress (MPa)	Fluid pH	Fracture RMS roughness (um)
1	2.5	7	3.80
2	2.5	5	3.80
3	5.0	7	3.80
4	5.0	5	3.80
5	10	7	3.80
6	2.5	7	8.27
7	2.5	5	8.27
8	5.0	7	8.27
9	5.0	5	8.27
10	2.5	6	3.80
11	5.0	6	3.80
12	2.5	6	8.27
13	5.0	6	8.27
14	2.5	7	3.80
15	2.5	8	3.80
16	2.5	7	8.27
17	5.0	7	8.27

The confining cell applies a constant isotropic confining stress (ranging from 2.5 to 10.0 MPa) throughout each individual test. Both reservoirs are connected to the core holder and nitrogen tank by flexible plastic tubing. Pore fluid flow rate is determined by measuring the mass of downstream reservoir throughout the experiment. The average permeability of the samples and effective hydraulic apertures of the sample fracture is determined by

measuring the volumetric flow rate of fluid with a fixed viscosity through the core sample of known geometry maintained at a fixed hydraulic gradient of 4.0 MPa/m over the sample (0.2 MPa gage pressure in the upstream reservoir and open to the atmosphere in the downstream reservoir). De-gassed double distilled water is used for the permeant at inlet pH 7 while a 1.76 mM and 0.176 M ammonium chloride solution are used for the permeant at inlet pH 6 and 5, respectively.

3.2 Effluent Fluid Calcium Ion Concentration

To measure the effective hydraulic aperture velocity in a way independent from the flow-through permeability tests, the effluent calcium concentration is measured in the permeating fluids. Long-term tests are also performed to measure the fully saturated calcium ion concentrations by leaving a section of the core in a bath of the respective fluid that is periodically stirred for a period of thirty days. Fluid samples, collected directly from the effluent side of the core sample, allow for the calcium concentration in the fluid to be profiled as a function of the fluid flow rate through the carbonate fracture using the Perkin-Elmer Optima 5300DV ICP-AES. They are taken during the permeability evolution experiments where confining stresses are maintained at 2.5, 5.0, and 10.0 MPa throughout the entire experiments (with all other experimental parameters identical) to determine the role of confining stress on the effluent fluid concentration of calcium ions. Theoretical effective fracture aperture velocities are calculated assuming that mineral mass was uniformly removed from 100 % of the fracture surface using Eq. (1) where C_{effl} is the mineral mass concentration (kg/m^3) in the permeating fluid, Q is the permeating fluid flow rate through the sample (m^3/s), ρ is the density of the mineral matter (kg/m^3), and D and L are the geometric width and length of the fracture (m), respectively.

$$\dot{\mathrm{b}} = \frac{C_{\mathrm{effl}} Q}{\rho D L} \tag{1}$$

We use Eq. (1) as a first approximation to response and refine this later, in light of detailed experimental observations. However, preferential dissolution of a narrow through-going channel by highly reactive fluid flow can result in fracture permeability evolution similar to that of well-distributed fracture flow of the same fluid. Meanwhile dissolution constrained to a small portion of the fracture surface results in significantly depressed fluid residence times and dissolved calcium concentrations. This may result in under-estimation of permeability-derived rates of fracture retreat calculated by the concentration of dissolved calcium and fluid flow rates while using Eq. 1 during highly channelized flow.

3.3 Fracture Topography Measurements

The topography of the fracture walls is measured both before and after an experiment with a white light interferometer (Wyko NT1100) using its widest field of view ($3.7 \times 4.9\,\mathrm{mm}^2$). Since the Capitan Massive Limestone used here is not sufficiently reflective for wide-field surface scans, metal surface castings of the walls are taken using an indium-containing low-temperature casting alloy that wets the carbonate surface as shown in Fig. 2.

Small field scans ($227 \times 299\,\mu\mathrm{m}^2$), for which the carbonate surface is sufficiently reflective to allow data collection, confirm that the metal castings accurately represent small features of the carbonate surface. Both wide-field and small field scans have a resolution of 736×480 data points per scan resulting in a resolution of 51 and 0.19 square microns per data point, respectively. Topographic inversion of the data is used to depict the original fracture surface

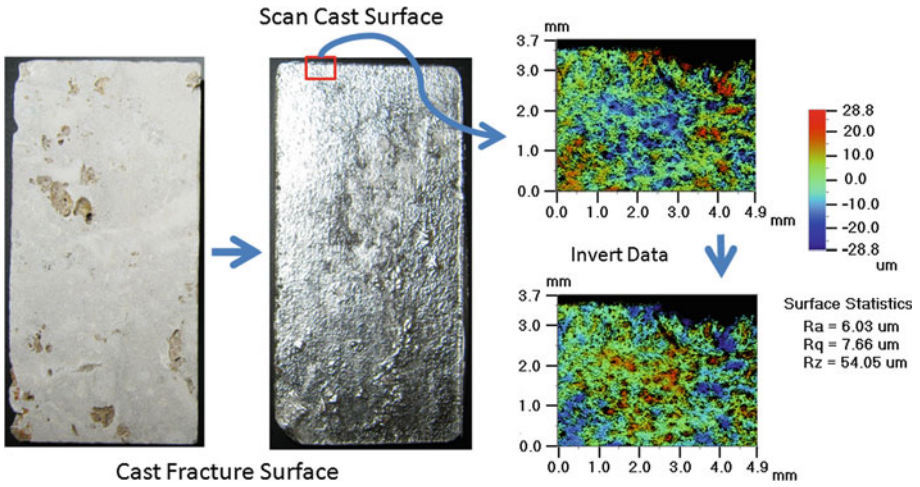

Fig. 2 Wide-field roughness measurement process of the carbonate fracture

rather than the surface "negative" given by the casting. Figure 2 shows this process from the carbonate sample all the way to the inverted topographic data. The box shown on the cast surface is approximately equal to the actual area of one large-field surface scan that is used for our analysis below.

4 Experimental Results

Flow-through permeability and effluent fluid calcium ion concentration measurements are performed on both closing and gaping fractures allowing for the characterization of the transition point between these two reactive flow regimes. The samples are maintained at a constant pore fluid pressure gradient while measuring the fluid flow rate to characterize the permeability of the fracture. Meanwhile white light profilometry measurements characterize the fracture wall topography and the approximate geometry of fracture-bridging asperities. These tests allow three factors of interest to be examined for their influence on fracture permeability evolution: the effective confining stress, the initial fracture roughness, and the acidity (pH) of the fluid permeating the fracture.

4.1 Flow-Through Permeability Measurements

The effective hydraulic aperture is derived using the cubic law expressed in Eq. (2) where b is the effective hydraulic aperture (m), D is sample diameter (m), and k_{eff} is the effective permeability (m^2) of the core evaluated from applying Darcy's law to flow within the sample.

$$b = \sqrt[3]{3\pi D k_{\text{eff}}} \tag{2}$$

The effective permeability of the entire cylindrical sample (k_{eff}) is expressed in Eq. (3) where dP is the fluid pressure differential across the sample (Pa) and μ is the dynamic viscosity of the permeating fluid (Pa s) while all other parameters have been previously defined.

$$k_{\text{eff}} = \frac{4Q\mu}{\pi D^2} \frac{L}{dP} \tag{3}$$

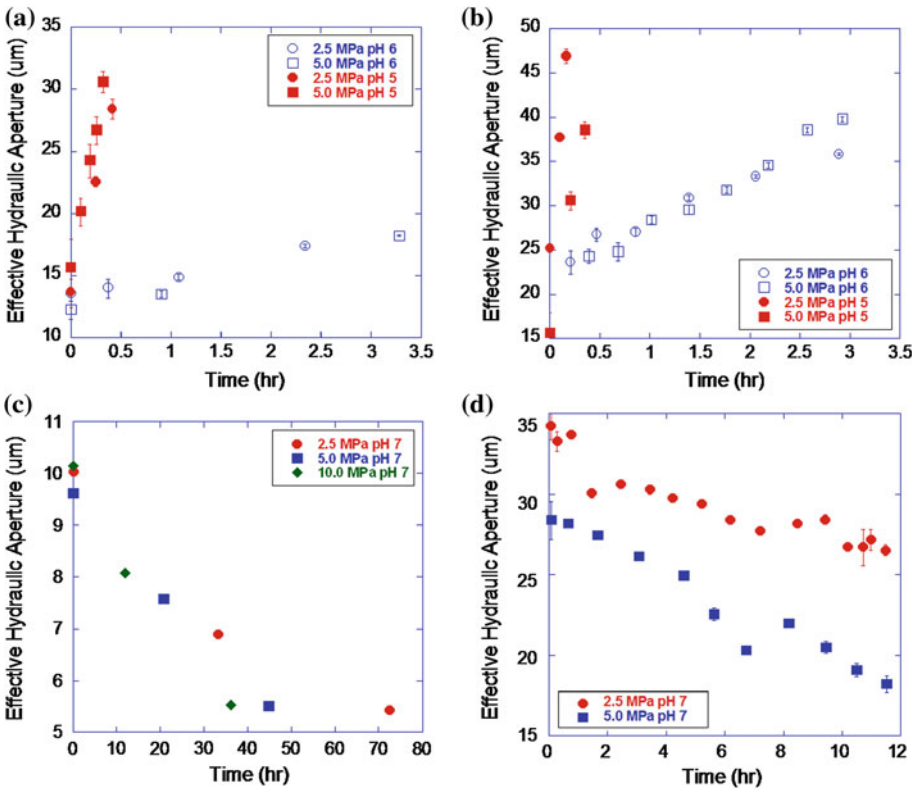

Fig. 3 Evolution of permeability derived hydraulic aperture of fractures in Capitan Massive limestone during flow-through tests with pH 5/6 (**a, b**) and pH 7 (**c, d**) fluid after fracture preparation with 150 grit (**a, c**) and 60 grit (**b, d**) ceramic abrasive

Figure 3 shows the effective hydraulic aperture plotted with respect to time for the experiments performed during the course of this study. Error is calculated based on the accuracy of the downstream fluid reservoir mass balance ($+/-5$ g)—only leading to significant error when characterizing low flow rates at short sample time intervals. These results show that a switch from pH 7 fluid flow to pH 6 fluid flow results in the transition from a closing to a gaping effective hydraulic aperture.

To gain a more detailed understand of mechanisms that contribute to the long-term fracture behavior additional pH 7 experiments are conducted and run until a steady-state effective hydraulic aperture is reached. Figure 4 shows this experimental data.

Both the rate and extent of fracture compaction prior to achieving a steady-state condition are different between the 60 and 150 grit prepared fractures during flow of pH 7 fluids, providing insight on relevant processes involved.

4.2 Effluent Fluid Calcium Concentration Measurements

To constrain the fracture permeability evolution in two ways, the effluent calcium concentration is monitored throughout the tests using fluid with pH 7 and 5. Results, displayed in Fig. 5, show two trends.

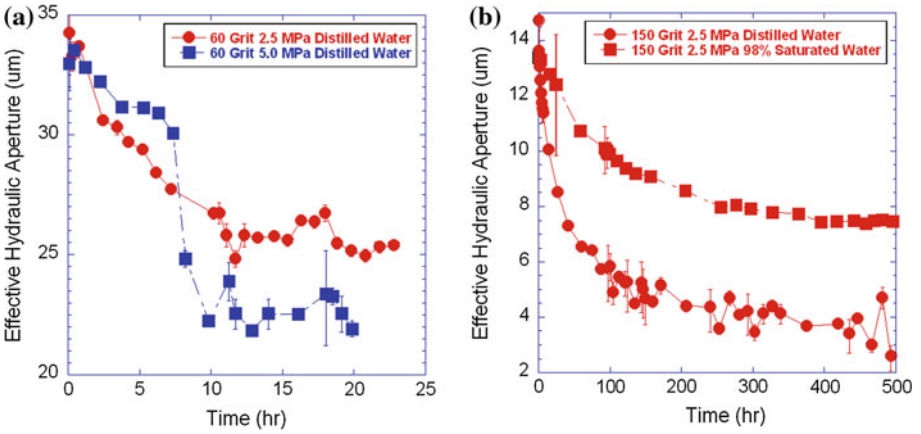

Fig. 4 Fracture permeability tests showing the steady-state effective hydraulic apertures of both (**a**) 60 grit and (**b**) 150 grit prepared fractures during pH 7 fluid flow

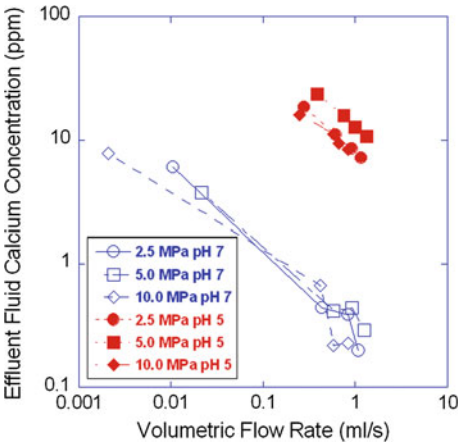

Fig. 5 Effluent fluid calcium concentration versus the volumetric flow rate of the fluid through 150 grit prepared samples

First it shows that the mass removal rate is greatly enhanced by lowering the fluid pH and that mass removal rate roughly scales with the concentration of hydronium (acid) ions. Secondly the effluent calcium concentration is well below the saturation limits measured for each condition (32.5 $mg_{Ca}/kg_{solution}$ for pH 7 fluid and 114 $mg_{Ca}/kg_{solution}$ for pH 5 solution) indicating a net dissolving fracture system in all cases. When the calcium concentration measurements, shown in Fig. 5, are used with Eq. 1 completely independent measurements of the effective hydraulic aperture velocity can be derived. Figure 6 shows that there is agreement between the permeability and mass flux-derived fracture aperture evolution.

Lower values of the effective hydraulic aperture velocities given by the mass flux compared to the permeability are due to the small fracture contact area. Fracture propping asperities represent a small portion of the fracture surface. Therefore assuming all mineral mass is preferentially removed from either fracture propping asperities or the fracture free-face will consistently under-predict observed permeability-derived effective hydraulic aperture velocities.

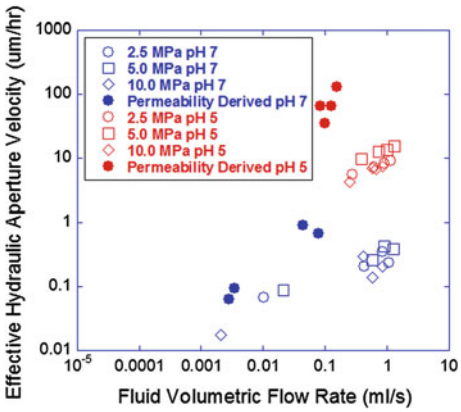

Fig. 6 Permeability- and mass flux-derived fracture aperture velocity both plotted with respect to fluid volumetric flow rate through the fracture

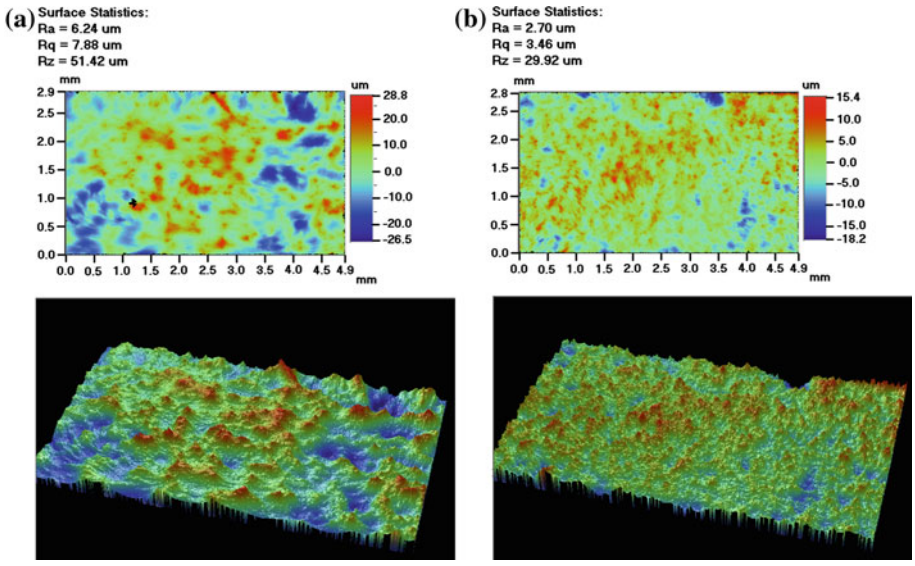

Fig. 7 Profilometry measurement of an (**a**) 60 grit and (**b**) 150 grit prepared fracture wall

4.3 Fracture Topography Measurments

A single sample of each of the fracture surfaces prepared by 60 and 150 grit abrasives are characterized by White Light Interferometry. Six percent of the fracture surface is scanned in six 3.7 by 4.9 mm patches before statistical analysis is used to calculate the expected surface roughness of the entire fracture surface. Figure 7 shows an example of the topographic data over a domain of approximately fifteen square millimeters for fracture surfaces prepared by both 60 and 150 grit abrasive.

Table 2 shows the average roughness (R_a), the root mean square roughness (R_q) and the average of the ten largest peak-to-valley measurements (R_z) together with their respective 95 % confidence interval errors of the fracture surfaces prior to fracture strain testing. Furthermore, the approximate diffusive radius, defined as the distance from the center of a hemispherical asperity to the advection-controlled pore space, is derived by measuring the average number of times the fracture surface intersects the zero displacement plane. These

Table 2 Statistical description of the fracture surfaces

	60 Grit	150 Grit
R_a (μm)	6.58	2.98
95 % C.I. error (μm)	0.81	0.28
R_q (μm)	8.27	3.80
95 % C.I. error (μm)	0.96	0.35
R_z (μm)	55.35	30.27
95 % C.I. error (μm)	4.63	4.54
Average number of X and Y axes crossings (/mm)	4.03	7.30
95 % C.I. error (/mm)	0.35	0.67
Resulting diffusion radius (μm)	248.1	137.0
95 % C.I. error (μm)	23.6	13.8

measurements are performed in both the x and y directions for both 60 and 150 grit surfaces prior to their use in experiments.

Statistical analysis shows that the roughness and diffusive radii of the synthetically prepared fracture surfaces is relatively uniform. Because of the uniform roughness and diffusive radii, and absent any significant long wavelength roughness effects, we hypothesize that the average fracture aperture is controlled by these microscopic fracture asperities rather than macroscopic topographic features. This information is used to constrain the model.

To complement the quantitative observations made with the intereferometer, select regions of the fracture walls were imaged after the experiments with an SEM. Though we did not identify clear indications of pressure solution or free-face dissolution, we were able to confirm that the grain size ranges between one and 10 μm, as indicated by the interferometer. Furthermore, the images show that the effective reactive surface of the fracture surface significantly exceeds the nominal fracture surface area as observed by White and Peterson (1990).

4.4 Effects of Fluid Reactivity

Fracture strains are measured to change from net compaction to net gaping when fluid with increased reactivity (pH decreased from 7 to 6) is circulated (Figs. 3, 5). By further increasing the fluid reactivity in separate but otherwise identical experiments (fluid pH decreased to 5) the rate of effective hydraulic fracture aperture growth increases close to an order of magnitude over that observed during pH 6 fluid circulation and effluent calcium concentration increases nearly two orders of magnitude over that observed during pH 7 fluid circulation. These both agree with the theory that the hydronium ions are the main control on mineral free-face dissolution leading to wormholes in carbonate–water systems. By measuring the calcium concentration during flow of fluids at both pH 5 and 7 at confining stresses ranging from 2.5 to 10 MPa, the calcium concentration is only observed to change as a function of fluid pH (Fig. 5) indicating that free-face dissolution represents the majority of the mineral mass transfer from the fracture surface.

4.5 Effects of Stress

A necessary requirement in following the evolution of aperture due to dissolution and precipitation is to correctly identify the initial aperture of the fracture as it is first loaded. We observe that the micro-scale fracture roughness controls the initial effective hydraulic

aperture, as evident in the similarities in initial permeabilities for all fractures prepared with a common small wavelength roughness (i.e., single diameter abrasive). We assume a theoretical unconfined uniaxial yield stress of crystalline carbonate to be on the order of 1.0 GPa (Hudson 1993). At effective asperity stresses greater than this, the fracture aperture decreases until the average fracture contact stress reaches the yield stress of the carbonate.

The confining stresses in our experiments are much lower than the critical stress, the theoretical minimum effective stress required for pressure solution to become active, for calcite at 20 °C ($\sim$ 199 MPa). This value is derived using Eq. 4. E_m represents the enthalpy of fusion for the mineral (36.0 kJ/mol for calcite) in the system, T and T_m are the temperature of the system and the melting temperature of the mineral (1,603 K for calcite) respectively, and V_m is the molar volume of the mineral (3.7E-5 mol/m^3 for calcite) (Yasuhara and Elsworth 2006; Lide 2008).

$$\sigma_{crit} = \frac{E_m \left(1 - \left(\frac{T}{T_m}\right)\right)}{4V_m} \tag{4}$$

Instead, we propose that stress corrosion cracking greatly enhances the active surface area of the fracture-propping asperities. Mass is then removed from these asperities at rates limited by molecular diffusion through the fluid film at the asperity contact. Relatively high reactive surface area maintains a saturated calcium concentration at the center of the asperity contact while the combination of short fracture length and high fluid advection maintains an under-saturated fluid concentration in the pore space adjacent to the asperity contact. This is compared to pressure solution where super-critical stress drives the concentration of dissolved calcium at the center of the asperity over the saturated value. Long-term fracture compaction rates in stress corrosion dominated fracture evolution decrease through time as a result of both the increasing contact radius of the assumed hemispherical fracture asperities and increased calcium concentration in the pore space resulting from decreased fluid advection rates.

4.6 Summary of Observations and Mechanisms

Principal observations are that fracture closure occurs (i) only where dissolution is not dominant (pH 7) and that (ii) the rate of closure increases with an increase in applied stress. That closure rate increases with an increase in applied stress is consistent with stress-mediated dissolution (pressure solution) as a dominant mechanism. However, since rates of both pressure solution and free-face dissolution scale uniformly with the dissolution rate coefficient, k_+, the masking of pressure dissolution effects at lower pHs is anomalous. We explain this inconsistency by invoking a hydrodynamic control that retards dissolution of the propping asperities. In this, mass removal is retarded from the dissolving asperity by the presence of a stagnant flow zone (zero-advection) that rings each asperity contact. The mass transport in this fluid zone is solely by diffusion and rate limits the removal of mass from the asperity and into the active advective flow field within the fracture. We quantify this model in the following.

5 Mechanistic Model

We present below a lumped parameter model to explore the experimental results. The principal constraining observations are the evolution of fracture aperture (as determined by

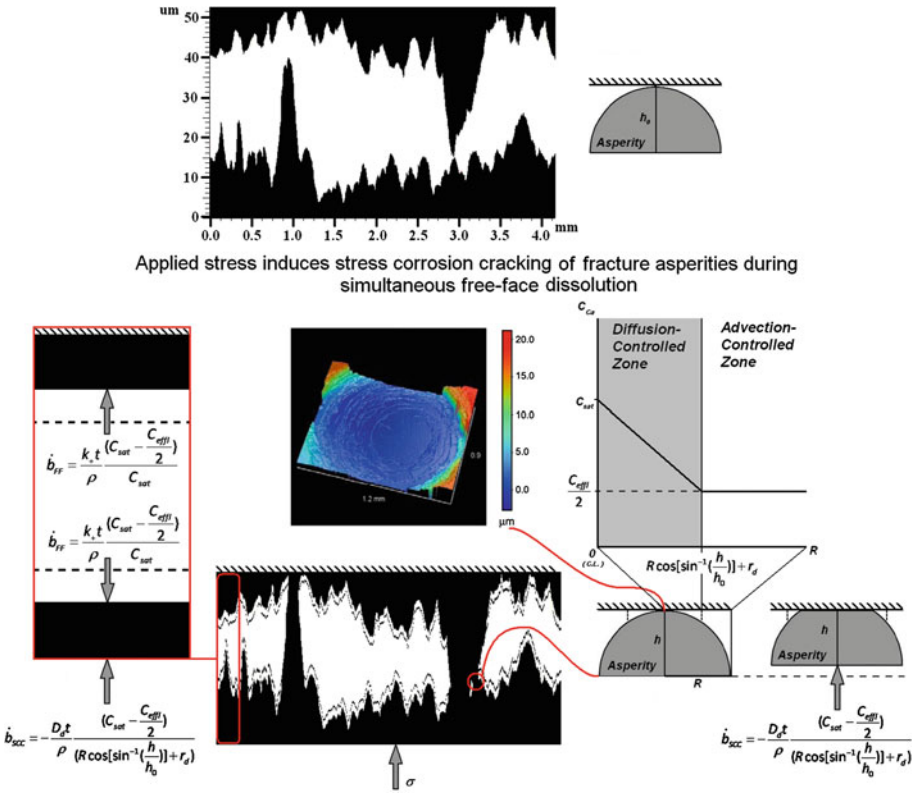

Fig. 8 Schematic of processes included in the model. *Top* Fracture profile prior to mechanical loading and assumed hemispherical model of a single asperity. *Bottom center* Approximate loaded fracture profile. *Bottom left* Free-face dissolution and its control on free-face retreat of the fracture surfaces. *Bottom right* Preferential dissolution of bridging asperities induced by micro-crack (stress corrosion)-enhanced surface area (*center*) and limited by molecular diffusion through the stagnant fluid halo showing evolving contact area. One-dimensional fracture hydraulic aperture velocities are due to free-face dissolution ($\dot{b}_{\mathrm{FF}}$) and due to stress corrosion cracking-induced diffusion ($\dot{b}_{\mathrm{SCC}}$) (Timms et al. 2010)

the permeability measurements) and the concentration of the effluent fluid, under different applied conditions of fracture roughness, ambient stress, fluid flow rate, and fluid reactivity. The principal features represented by the model are identified schematically in Fig. 8.

5.1 Dominant Mineral Mass Transport Mechanisms

The dominant mass transport mechanism at the fracture surface is determined by considering the diffusive and advective flow regimes adjacent to the fracture contact. Fluid flow is assumed to be laminar throughout the fracture due to the low value of the Reynolds number ($Re << 100$). Constant-pressure boundary conditions are prescribed at the upstream and downstream edges of the fracture, and a no-slip boundary condition-imposed across the fracture. Thus, the flow velocity profile is defined by Eq. 5 from the fracture wall to the center of the fracture aperture (at $r_d = \frac{b}{2}$), where V is the local fluid velocity, r_d is the distance from the dissolving wall, V_{a} is the average flow velocity across the entire fracture aperture, and b is the effective hydraulic aperture.

$$V = \frac{8V_a r_d^2}{b^2} \tag{5}$$

The Peclet number, *Pe*, is the ratio of advective to diffusive fluxes, and given by Eq. 6 where D_d is the diffusion coefficient of the mineral being dissolved.

$$Pe = \frac{V_c r_d}{D_d} \tag{6}$$

Diffusive transport will dominate over advective transport where the Peclet number falls below unity. Thus, setting the Peclet number to unity enables a critical local velocity, V_c, to be determined, below which diffusion is the dominant mass transport mechanism. Substituting the local velocity (V) from Eq. 5 into the critical velocity (V_c) from Eq. 6 enables a threshold critical fracture aperture (b_{crit}) to be determined in Eq. 7, where L is the geometric length of the sample (fracture), μ is the dynamic viscosity of the permeating fluid, and dP is the pressure differential over the sample.

$$b_{crit} = 2r_d = \sqrt[3]{\frac{12D_d L\mu}{dP}} \tag{7}$$

This model assumes that diffusion is the dominant mass transport mechanism at and around fracture contacts where the aperture is less than the critical fracture aperture. Beyond these zones, where the aperture is greater than the threshold, mass transport is assumed to be controlled by advection (Fig. 8).

5.2 Free-Face Dissolution

At fracture apertures greater than twice the diffusion-controlled half-aperture the predominant mineral mass transport mechanism will be free-face dissolution. In these zones the mass removal rate is controlled by the rate at which hydronium ions bond to surface carbonate groups, thus forming bicarbonate ions that can diffuse away from the mineral surface. Consequently, as the concentration of the hydronium ions increases (i.e., pH decreases) the free-face dissolution rate, k_+, increases. Previous research has quantified these rates at 10^{-8} to 10^{-6} kg/m^2-s for pH 7–5 fluids (Plummer et al. 1978). These values of k_+ are multiplied by 7 to reflect the mean measured ratio of the BET surface area to the nominal (macroscopic geometric) surface area (that is measured to vary between 1.08 and 15) as published by White and Peterson (1990). The free-face dissolution-induced mass flux ($\dot{M}_{FF}$) is expressed by Eq. 8 where A is the reactive fracture surface area, k_+ is the mineral dissolution rate coefficient, and the driving force term is represented by a term that includes the observed effluent fluid calcium concentration (C_{effl}) and the saturated calcium concentration (C_{sat}). The expression for the retreat velocity of the fracture free surface ($\dot{b}_{FF}$) includes the time step increment of the model (t) and the density of the mineral (ρ). The concentration of effluent calcium is divided in half in the driving force term to represent the approximate fracture length averaged driving force in one lumped-parameter term.

$$\dot{M}_{FF} = Ak_+ \frac{\left(C_{sat} - \frac{C_{effl}}{2}\right)}{C_{sat}} \tag{8}$$

$$\dot{b}_{FF} = \frac{2k_+ t}{\rho} \frac{\left(C_{sat} - \frac{C_{effl}}{2}\right)}{C_{sat}} \tag{9}$$

5.3 Stress-Induced Dissolution

Pressure solution does not contribute significant mass flux to the permeating fluid as shown by insignificant change in the calcium concentration with changing fracture stress in Fig. 3. Therefore stress corrosion cracking is assumed to operate as the only mechanism of asperity destruction (fracture compaction) in the contact model. Specifically, stress corrosion cracking is assumed to be limited by the rate of mass diffusion from the stressed asperities. We assume that mass is removed uniformly over the entire asperity contact, so that the rate of mass flux resulting from stress corrosion cracking-induced diffusion can be evaluated over a given asperity contact. This mass removal rate ($\dot{M}_{\mathrm{SCC}}$) and the resulting uniform fracture closure velocity ($\dot{b}_{\mathrm{SCC}}$) are defined in Eqs. 10 and 11 where A is the area of the contact undergoing stress corrosion cracking, D_d is the diffusion coefficient of the mineral, R is the maximum radius of these quasi-hemispherical asperities (taken to be 137 μm for the 150 grit surfaces and 250 μm for the 60 grit surfaces) with an assumed initial height equal to the maximum simulated fracture aperture prior to mechanical loading (h_0). h is the height of the maximum fracture aperture after mechanical loading and at each time step as free-face dissolution and stress corrosion alter the fracture aperture.

$$\dot{M}_{\mathrm{SCC}} = A D_d \frac{\left(C_{\mathrm{sat}} - \frac{C_{\mathrm{effl}}}{2}\right)}{\left(R\cos\left[\sin^{-1}\left(\frac{h}{h_0}\right)\right] + r_d\right)} \tag{10}$$

$$\dot{b}_{\mathrm{SCC}} = -\frac{D_d t}{\rho} \frac{\left(C_{\mathrm{sat}} - \frac{C_{\mathrm{effl}}}{2}\right)}{\left(R\cos\left[\sin^{-1}\left(\frac{h}{h_0}\right)\right] + r_d\right)} \tag{11}$$

This formulation assumes that as the aperture closes due to stress corrosion, both the diffusion length across the asperities and the concentration of calcium in the effluent fluid increases as a consequence of longer fluid residence times due to decreased average laminar fluid flow velocities. With the assumed boundary condition of fully saturated fluid at the center of the contacting asperities, the increased effluent calcium concentration in the fluid at lower flow rates (smaller effective hydraulic apertures) leads to smaller dissolved calcium concentration gradient in the diffusion-controlled asperity contact zone. Fick's law dictates that with a longer diffusion length and lower concentration gradient the rate of stress corrosion induced fracture closure decreases at lower effective hydraulic apertures.

5.4 Ensemble Model

This lumped parameter model assumes that the entire fracture aperture closes at a rate proportional to the induced strain rate ($\dot{b}_{\mathrm{SCC}}$) due to stress corrosion cracking—and that this rate is diffusion-controlled. The architecture of the pores within the fracture is controlled by the micro-scale roughness. At fracture apertures less than b_{crit}, stress corrosion-induced fracture strain is the only mechanism assumed to significantly contribute to the evolution of the pore space. Meanwhile, at fracture apertures greater than b_{crit}, free-face dissolution is assumed to induce a uniform fracture face retreat (gaping), while stress corrosion cracking-induced diffusion leads to negative fracture aperture strain (closure). Therefore, the relative rates of these two processes averaged over the entire fracture length will lead to either increases or decreases in the fracture aperture with time.

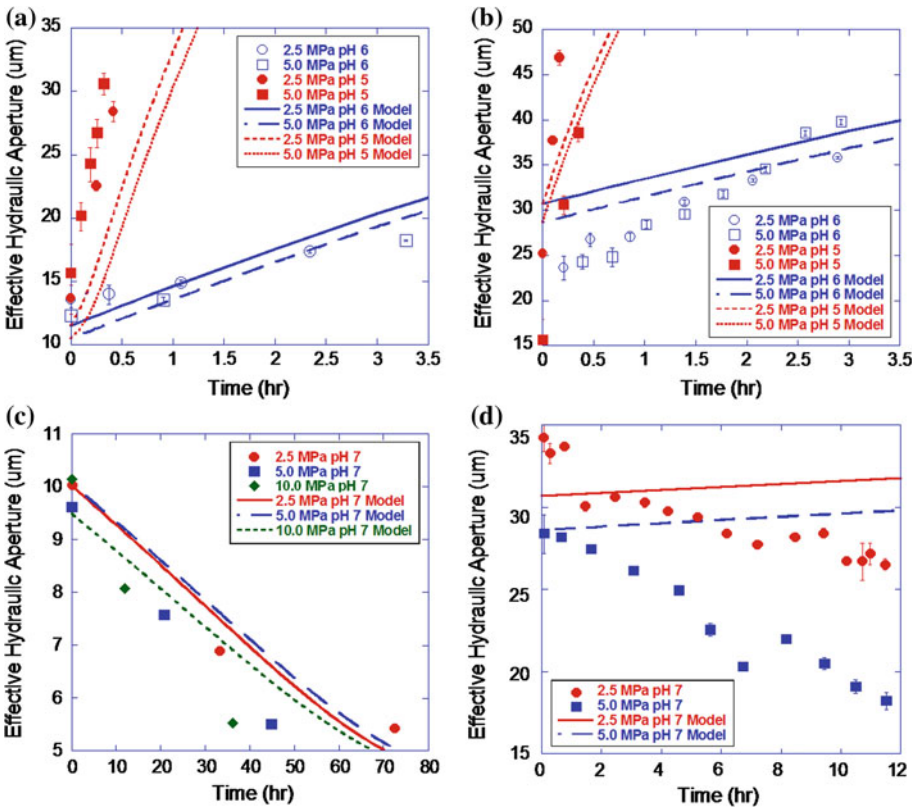

Fig. 9 Experimentally measured (*points*) and simulated (*lines*) evolution of effective hydraulic aperture of fractures in tight carbonate material during flow-through tests with pH 5 and 6 (**a, b**) and pH 7 (**c, d**) fluid after fracture preparation with 150 grit (**a, c**) and 60 grit (**b, d**) ceramic abrasive

6 Simulation Results

The model presented is constrained by a combination of theoretical parameters and the experimental measurements of the concentration of dissolved minerals in the permeating fluid with respect to fluid flow rate through the fracture. Resulting values of average fracture aperture evolution are applied to the parallel plate flow model that determines the volumetric fluid flow rate through the system via the cubic law (Eq. 2).

6.1 Initial Fracture Aperture

The initial average fracture aperture predicted by the method described in Sect. 3.5 (for a 150 grit prepared surface) is nearly identical to those observed in our experiments at between 9.5 and 11.5 μm, depending on the confining stress. Initial average hydraulic apertures predicted for 60 grit prepared fractures are also very similar to those observed in our experiments (Fig. 9). However, the larger fracture roughness and greater amount of uncertainty in the roughness results in a greater variance between the predicted and measured initial apertures (Fig. 9).

6.2 Fracture Aperture Evolution

The model results are plotted alongside the experimental results in Fig. 7, and show a reasonable fit. During the flow of low reactivity fluids (pH 7) initially smooth fractures are predicted to close at rates similar to those observed in experiments. As fluid reactivity increases (pH 6 and 5 fluids), both model and experiments indicate increasing rates of fracture gaping. However, for initially rough fractures (60 grit) permeated by near neutral (pH 7) fluid, the model does not predict accurately the experimental results, as it indicates gaping rather than closing. These experiments contain periodic step decrements in the effective hydraulic aperture that are neither included in the mechanistic framework of the model nor in the resulting predictions. These cumulative effects result in the poor fit between model and observations.

7 Analysis

The lumped parameter model presented in this paper has adequately represented the effects of stress corrosion cracking-induced diffusion and free-face dissolution on the permeability of stressed fractures permeated by reactive fluids. The model failed to predict the behavior of the system in the case of a neutral pH fluid flowing through 60 grit fractures. We use these results to extend our understanding of processes leading to fracture permeability evolution.

7.1 Stress Corrosion Cracking-Induced Diffusion and Pressure Solution

Pressure solution is only active under local stresses greater than the critical stress ($\sim$ 199 MPa for calcite). Therefore pressure solution may dominate the early response, when the local stresses are high, but our experimental data indicates that pressure solution mass flux is insignificant late in our tests. As the fracture closes, local contact area grows and local stresses decrease, so that the effect of pressure solution diminishes, and stress corrosion cracking-induced diffusion emerges as the dominant process (Fig. 10b). Stress corrosion cracking results in preferential dissolution of locally stressed fracture asperities due to the enhanced surface area induced by subcritical crack growth. Mass transfer rates in this regime are characterized by diffusion through the water film between asperities, with the maximum concentration capped at the saturation of calcite in water at the center of the asperity and the concentration equal to that of the bulk permeating fluid at the edge of the asperity. As fracture aperture further closes (albeit at a reduced rate), flow rates through the fracture decrease, aqueous concentrations build and diffusive mass transport from the asperity contacts slows as the overall concentration gradient is reduced. Thus, the highest concentration gradient under pressure solution reduces to a lower concentration gradient during stress corrosion cracking and finally to a very small gradient as ultimately pore water concentrations build (Fig. 10b).

For the fracture prepared with fine (150 grit) ceramic pressure solution is predicted to be active down to a minimum hydraulic aperture of 8 μm at a confining stress of 10 MPa. Conversely, the coarse (60 grit) ceramic prepared fractures experience effective asperity stresses beyond the critical stress throughout the short-term experiments. These predictions of super-critical effective stresses experienced by the fracture-propping asperities explain the differences between the model that does not include pressure solution and our experimental results.

The only major difference between the model and the experimentally measured trends is that during the flow of neutral fluid (pH 7) through an initially rough (60 grit prepared)

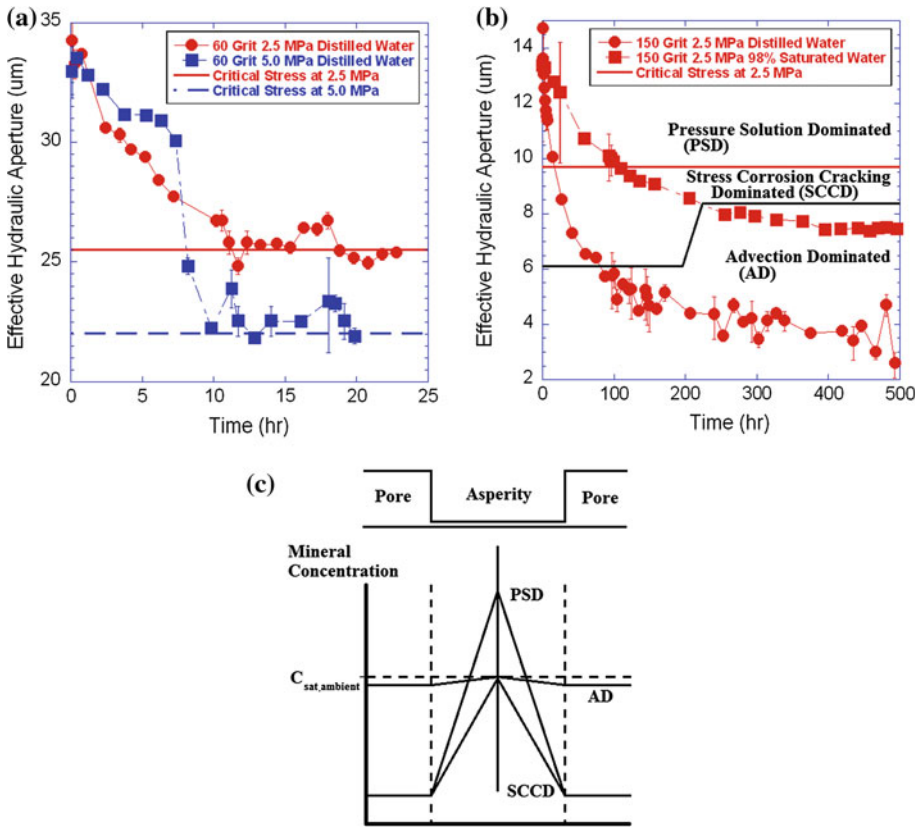

Fig. 10 Fracture permeability tests showing the steady-state effective hydraulic apertures of both (**a**) 60 grit and (**b**) 150 grit prepared fractures during pH 7 fluid flow. *Lines* are placed at the effective hydraulic aperture where the effective stress on fracture asperities is predicted by our model to be equal to the critical stress for pressure solution. Fluid saturation profiles across a theoretical asperity are shown (**c**) for pressure solution dominated (PSD), stress corrosion cracking dominated (SCCD), and advection-dominated (AD) fracture evolution

fracture, multiple sudden drops in a decreasing effective hydraulic aperture are recorded. The model predicts a slowly gaping hydraulic aperture due to the longer asperity diffusion radius and resulting lower concentration gradient in the diffusion-controlled zone compared to that of the 150 grit prepared fracture. We conjecture that pressure solution elevates the calcium concentration gradient in these loaded asperity contacts and induces the experimentally observed fracture closure in the 60 grit experiments (Fig. 10c). Figure 10 shows the experimental data from Fig. 5 with lines added to indicate the effective hydraulic aperture when the fracture propping asperities are expected to transition from a state of super-critical to sub-critical stress.

These results indicate that most of the fracture closure observed in pH 7 experiments can be attributed to pressure solution of the asperity to a slender column that collapses plastically, similar to observations by Karcz et al. (2008). Asperity shortening by stress corrosion cracking-induced diffusion causes continued closure at rates well-predicted by our model for initially smooth fracture walls. Rough (60 grit) fractures quickly reach an effective steady-state in terms of the hydraulic aperture, where fracture aperture oscillates between

closure due to pressure solution and gaping by free-face dissolution dominating the rate of stress corrosion cracking-induced fracture closure. Absent the pressure solution-induced effects, the lumped parameter stress corrosion model accurately represents the experimental observations of fracture closure during percolation of undersaturated pH 7 pore fluid.

7.2 Free-Face Dissolution

The model accurately predicts rates of fracture gaping during flow of reactive fluids (pH 6–5). However, to match the experimentally observed rates of aperture gaping we assume that the effective surface area of the fracture is approximately seven times greater than the nominal area (product of length and diameter) of the fracture surface. This larger assumed surface area is consistent with SEM images and previous research indicating that the BET surface area of reactive mineral surfaces are 1.08–15 times larger than the nominal surface area, with a mean of approximately 7 (White and Peterson 1990). Highly reactive fluids-induced fracture free-face retreat at a rate proportional to the product of the effective surface area and the chemical dissolution rate coefficient.

7.3 Ensemble Fracture Permeability Evolution

To explain the contrasting behaviors of long-term permeability change observed here we explore contrasting modes of mineral dissolution. Both systems remain chemically undersaturated with respect to calcite throughout the experiments, so that the system is in a state of net dissolution. We consider a dimensionless mass flux ratio ($\chi = \frac{\dot{M}_{\mathrm{FF}}}{\dot{M}_{\mathrm{SCC}}}$) to express the ratio of free-face to stress-corrosion-induced mass fluxes within a stressed fracture permeated by reactive fluid where stress-induced ($\chi < 1$) or free-face dissolution ($\chi > 1$) effects dominate: defined in Eq. (12).

$$\chi = \frac{Ak_{+}\frac{\left(C_{\mathrm{sat}} - \frac{C_{\mathrm{eff}}}{2}\right)}{C_{\mathrm{sat}}}}{AD_d\frac{\left(C_{\mathrm{sat}} - \frac{C_{\mathrm{eff}}}{2}\right)}{(R+r_d)}} \tag{12}$$

The expression for $\dot{M}_{\mathrm{SCC}}$ is simplified to a more generalized form for use in the mass flux ratio. In addition, the mass flux ratio can be further simplified from Eqs. 12 to 13.

$$\chi = \frac{k_{+}(R + r_d)}{D_d C_{\mathrm{sat}}} \tag{13}$$

Comparing our experimentally measured effective hydraulic aperture evolution and that predicted by the mass flux ratio, we find that in most cases where $\chi > 1$ positive (gaping) effective hydraulic aperture velocities are the long-term fracture behavior. Meanwhile all cases where $\chi < 1$ negative (closing) effective hydraulic aperture velocities are measured as the long-term behavior. The only experimental data sets that refuted long-term fracture permeability behaviors predicted by the mass flux ratio are the rough (60 grit) prepared fractures permeated by pH 7 fluid. However, as discussed above, the difference between our predicted behavior and that measured is attributed to measuring the transient effects of pressure solution. Transition from closing to gaping fracture regimes logically occurs when the mass flux ratio is approximately equal to unity—indicating equal rates of mass removal from fracture propping asperities (via stress-corrosion-enhanced diffusion) and fracture free faces (via chemical dissolution).

8 Conclusions

In this study we explore the roles of stress, reactive chemistry, and fracture roughness on the evolution of permeability in fractures. We also use a lumped parameter model of a fracture supported by a series of propping asperities to represent the evolution of fracture aperture in fractures permeated by reactive fluids. Experimental measurements of the evolution of fracture aperture compare well with this lumped parameter model. This is particularly true at pH < 7 where the model accurately reflects free-face dissolution dominating diffusion-controlled stress corrosion cracking-induced compaction in a stressed carbonate fracture. As the fluid reactivity to the mineral decreases, the rate of fracture free-face retreat approaches the rate of fracture compaction by stress corrosion cracking-induced diffusion leading to eventual steady-state effective hydraulic fracture aperture values. As fracture roughness increases we propose that fracture contact area is low enough that stresses on fracture asperities exceeds the critical stress and we measure pressure solution-dominated fracture compaction for a significant portion of the effective hydraulic aperture evolution. This explains the error between the measured effective hydraulic aperture evolution of 60 grit prepared experiments permeated by pH 7 fluids and both that predicted by our lumped parameter model and the mass flux ratio.

This is also the first time that a repeatable and constrained set of experiments has been combined with simulations to precisely isolate that a transition from pressure solution to stress corrosion cracking-enhanced diffusion must take place to match observed rates of effective fracture hydraulic aperture compaction in stressed carbonates permeated by pH 7 fluid. It is the relative rates of fracture compaction from stress corrosion cracking-enhanced diffusion and gaping from free-face dissolution that determines the long-term permeability evolution of lightly stressed fractures permeated by reactive fluid. As a result, we propose a mass flux ratio—the ratio of free-face dissolution to stress-corrosion-enhanced dissolution—as an index to distinguish between mechanically and chemically mediated changes in permeability in these fractures. Discriminating these behaviors is important because the sense of permeability change, reduction versus enhancement, is different for each mechanism.

Acknowledgements We would like to thank ExxonMobil Upstream Research Company: Stratigraphic and Reservoir Systems division for their generous research grant.

References

Croizé, D., Renard, F., Bjørlykke, K., Dysthe, D.: Experimental calcite dissolution under stress: evolution of grain contact microstructure during pressure solution creep. J. Geophys. Res. (2010). doi:10.1029/2010JB000869

Daccord, G., Liétard, O., Lenormand, R.: Chemical dissolution of a porous medium by a reactive fluid—II. Convection vs reaction, behavior diagram. Chem. Eng. Sci. **48**, 179–186 (1993)

Detwiler, R.: Experimental observations of deformation caused by mineral dissolution in variable-aperture fractures. J. Geophys. Res. (2008). doi:10.1029/2008JB005697

Detwiler, R., Rajaram, H.: Predicting dissolution patterns in variable aperture fractures: evaluation of an enhanced depth-averaged computational model. Water Resour. Res. (2007). doi:10.1029/2006WR005147

Dijk, P., Berkowitz, B.: Precipitation and dissolution of reactive solutes in fractures. Water Resour. Res. **34**, 457–470 (1998)

Donohue, S., Sullivan, C., Long, M.: Particle breakage during cyclic triaxial loading of a carbonate sand. Géotech. (2009). doi:10.1680/geot.2008.T.003

Durham, W., Bourcier, W., Burton, E.: Direct observation of reactive flow in a single fracture. Water Resour. Res. 37(1), 1–12 (2001). doi:10.1029/2000WR900228

Hoeffner, M., Fogler, H.: Pore evolution and channel formation during flow and reaction in porous media. Am. Inst. Chem. Eng. **34**, 45–54 (1988)

Hudson, J.: Comprehensive Rock Engineering: Principles, Practice & Projects. Pergamon Press Ltd, Oxford (1993)
Kalia, N., Balakotaiah, V.: Effect of medium heterogeneities on reactive dissolution of carbonates. Chem. Eng. Sci. (2009). doi:10.1016/j.ces.2008.10.026
Karcz, Z., Aharonov, E., Ertas, D., Polizzotti, R., Scholz, C.: Deformation by dissolution of a single crystal sodium chloride indenter: an experimental study under the confocal microscope. J. Geophys. Res. (2008). doi:10.1029/2006JB004630
Lide, D.: CRC Handbook of Chemistry and Physics, 8th edn. CRC Press LLC., Boca Raton, FL (2008)
Panga, M., Ziauddin, M., Balakotaiah, V.: Two-scale continuum model for simulation of wormholes in carbonate acidization. Am. Inst. Chem. Eng. (2005). doi:10.1002/aic.10574
Plummer, L., Wigley, T., Parkhurst, D.: The kinetics of calcite dissolution in CO_2–water systems at 5 ° to 60 °C and 0.0 to 1.0 atm CO_2. Am. J. Sci. **278**, 179–216 (1978)
Polak, A., Elsworth, D., Yasuhara, H., Grader, A., Halleck, P.: Permeability reduction of a natural fracture under net dissolution by hydrothermal fluids. Geophys. Res. Lett. (2003). doi:10.1029/2003GL017575
Polak, A., Elsworth, D., Liu, J., Grader, A.: Spontaneous switching of permeability changes in a limestone fracture with net dissolution. Water Resour. Res. (2004). doi:10.1029/2003WR002717
Siemers, J., Dreybrodt, W.: Early development of karst aquifers on percolation networks of fractures in limestone. Water Resour. Res. **34**, 409–419 (1998)
Timms, N., Healy, D., Reyes-Montes, J., Collins, D., Prior, D.: Paul Young, R. Effects of crystallographic anisotropy on fracture development and acoustic emission in quartz. J. Geophys. Res. (2010). doi:10.1029/2009JB006765
Volery, C., Davaud, E., Durlet, C., Clavel, B., Charollais, J., Caline, B.: Microporous and tight limestones in the Urgonian formation (late Hauterivian to early Aptian) of the French Jura Mountains: focus on the factors controlling the formation of microporous facies. Sediment. Geol. (2010). doi:10.1016/j.sedgeo.2010.06.017
White, A., Peterson, M.: Role of reactive-surface-area characterization in geochemical kinetic models. ACS Symp. Ser. (1990). doi:10.1021/bk-1990-0416.ch035
Yasuhara, H., Elsworth, D.: A numerical model simulating reactive transport and evolution of fracture permeability. Int. J. Numer. Anal. Methods Geomech. (2006). doi:10.1002/nag.513
Yasuhara, H., Elsworth, D., Polak, A.: A mechanistic model for compaction of granular aggregates moderated by pressure solution. J. Geophys. Res. (2003). doi:10.1029/2003JB002536
Yasuhara, H., Elsworth, D., Polak, A.: Evolution of permeability in a natural fracture: significant role of pressure solution. J. Geophys. Res. (2004). doi:10.1029/2003JB002663
Yasuhara, H., Kinoshita, N., Ohfuji, H.: Sung Lee, D., Nakashima, S., Kishida, K.: Temporal alteration of fracture permeability in granite under hydrothermal conditions and its interpretation by coupled chemo-mechanical modeling. Appl. Geochem. (2011). doi:10.1016/j.apgeochem.2011.07.005
Zhang, X., Spiers, C., Peach, C.: Compaction creep of wet granular calcite by pressure solution at 28 °C to 150 °C. J. Geophys. Res. (2010). doi:10.1029/2008JB005853
Zhang, Y., Zhang, W., Yang, C.: FEM analysis for influences of stress corrosion and pressure solution on THM coupling in dual-porosity rock mass. Sci. China Tech. Sci. (2011). doi:10.1007/s11431-011-4437-6